# An Automated Approach to Estimating Convective Boundary Layer Depth from Dual-Polarization WSR-88D Radar Observations

C. Lyn Comer, Braedon Stouffer, David J. Stensrud, Yunji Zhang, And Matthew R. Kumjian C. Lyn Comer, Braedon Stouffer, David J. Stensrud, Yunji Zhang, And Matthew R. Kumjian C. Lyn Comer, And Matthew R. Lyn Comer, A

<sup>a</sup> Department of Meteorology and Atmospheric Science, The Pennsylvania State University, University Park, Pennsylvania

(Manuscript received 14 December 2023, in final form 30 May 2024, accepted 14 June 2024)

ABSTRACT: Convective boundary layer (CBL) depth can be estimated from dual-polarization WSR-88D radars using the product differential reflectivity  $Z_{\rm DR}$  because the CBL top is collocated with a local  $Z_{\rm DR}$  minimum produced by Bragg scatter at the interface of the CBL and the free troposphere. Quasi-vertical profiles (QVPs) of  $Z_{\rm DR}$  are produced for each radar volume scan and profiles from successive times are stitched together to form a time-height plot of  $Z_{\rm DR}$  from sunrise to sunset. QVPs of  $Z_{\rm DR}$  often show a low- $Z_{\rm DR}$  channel that starts near the ground and rises during the morning and early afternoon, identifying the CBL top. Unfortunately, results show that this channel within the QVP can occasionally be misleading. This motivated creation of a new variable DVar, which combines  $Z_{\rm DR}$  with its azimuthal variance and is particularly helpful at identifying the CBL top during the morning hours. Two methods are developed to track the CBL top from QVPs of  $Z_{\rm DR}$  and DVar. Although each method has strengths and weaknesses, the best results are found when the two methods are combined using inverse variance weighting. The ability to detect CBL depth from routine WSR-88D radar scans rather than from rawinsondes or lidar instruments would vastly improve our understanding of CBL depth variations in the daytime by increasing the temporal and spatial frequencies of the observations.

SIGNIFICANCE STATEMENT: The daytime convective boundary layer (CBL) can increase in depth from a few hundred to a few thousand meters between sunrise and sunset and is strongly connected to temperature changes at Earth's surface. Unfortunately, current observations of CBL depth primarily consist of measurements from twice daily rawinsonde launches at 97 locations across the United States. As a result, CBL depth observations lack fine spatial and temporal resolution and miss the daily cycle of CBL growth. This study seeks to fill the gaps in CBL depth observations by developing an automated method to estimate CBL depth from dual-polarization WSR-88D radar observations with a temporal resolution as fine as 5–10 min. These observations will greatly enhance our ability to observe and monitor CBL depth in real time.

KEYWORDS: Boundary layer; Radars/Radar observations; Pattern detection

#### 1. Introduction

The planetary boundary layer (PBL) is the atmospheric layer that directly interfaces with Earth's surface, with depths that can vary from a few hundred meters to a few thousand meters during the daytime (Stull 1988). The PBL can be subdivided into several vertical layers: the surface layer, the mixed layer, the entrainment zone, the residual layer, and the stable (nocturnal) boundary layer at various times during the diurnal cycle. The mixed layer is called the convective mixed layer or convective boundary layer (CBL) when the turbulence associated with it is driven by convective heat transfer from the surface, often leading to vertically wellmixed profiles of potential temperature  $\theta$ , water vapor mixing ratio  $q_{ij}$  and wind speed (Stull 1988). The CBL grows primarily via entrainment in which thermals rising from the surface overshoot the top of the CBL and mix air from the overlying free troposphere into the CBL (Wyngaard 1985). The top of the CBL is defined as the middle of the entrainment zone, which is characterized by large vertical gradients of  $\theta$ ,  $q_v$ , and wind speed (Stull 1988). The value of  $\theta$  increases within the

Corresponding author: David J. Stensrud, david.stensrud@psu.edu

entrainment zone, whereas in contradistinction,  $q_v$  decreases in the entrainment zone due to mixing with drier free tropospheric air. CBL depth depends on a variety of factors, including incoming solar radiation, surface sensible heat flux, horizontal thermal advection, large-scale vertical motion, local terrain features, the structure of the residual layer, and the presence of clouds. As a result, the structure and evolution of the CBL can have large daily variations and are influenced by location, atmospheric and land conditions, and season.

CBL depth impacts pollutant concentrations (Garc et al. 2002; Ching et al. 1988; Liu et al. 2020), convection initiation (Crook 1996; Browning et al. 2007), and precipitation amounts (Holzworth 1964; Johnson and Mapes 2001; Bright and Mullen 2002; McCaul and Cohen 2002). In addition, wildfire behavior and the diffusion of hazardous airborne materials can be influenced by boundary layer structure (Dabberdt et al. 2004; Clements et al. 2007; Erickson et al. 2016). Improved observations of CBL depth and evolution would impact forecasting and modeling of these crucial areas by providing insight into the structure of the boundary layer.

In the CONUS, CBL depth is the smallest on average in the winter months due to decreased solar heating of the surface and the largest in the summer months when greater surface fluxes encourage more vertical mixing and entrainment. Holzworth (1964) found that average CBL depths are the smallest in the months of December and January, ranging from 200 to 800 m, and the largest in May–August, reaching up to near 1600 m in most of the eastern United States and exceeding 3000 m in the Rocky Mountains. Along the Atlantic and Pacific coastlines, the average CBL is shallow and its depth does not vary greatly in fall and summer, likely due to the lower ocean temperatures impacting CBL growth (Holzworth 1964). Holzworth (1964) noted that there can be significant day-to-day variation in CBL depth, particularly in continental regions where the diurnal cycle of the CBL is strong. This observation suggests that CBL structure is an important feature that requires further study at a finer temporal scale.

The most readily available CBL depth estimates are obtained from rawinsonde data by measuring vertical gradients in  $\theta$  and relative humidity (RH). Unfortunately, rawinsondes are only launched twice daily at 0000 and 1200 UTC at 97 locations in the United States (U.S. Department of Commerce 2023). Additionally, rawinsondes provide a single vertical profile of observations along the balloon's ascending path which may not be representative of the surrounding area (Stull 1988). Lidar and wind profilers can be used to estimate CBL depth (White 1993; Angevine et al. 1994; Cohn and Angevine 2000), but these instruments typically are available only in field campaigns, limiting their availability for routine estimates of the CBL depth across the CONUS. Ceilometers also can provide CBL depth estimates by measuring aerosol backscatter profiles (Münkel et al. 2007). However, estimating CBL depth using ceilometers over a wide range of locations and stability conditions has proven to be difficult and requires further development (Zhang et al. 2022). Additionally, lidar ceilometers struggle to detect morning growth of the CBL since the gradients in aerosol concentration are weak in the CBL and instead are dominated by gradients at the top of the residual layer (Münkel et al. 2007). As a result, the currently available spatial and temporal resolution of CBL depth observations is less than ideal. Thankfully, dual-polarization WSR-88D radars have been shown to detect the top of the CBL as shown by Melnikov et al. (2011, 2013), Richardson et al. (2017a,b), and Banghoff et al. (2018) and have the potential to tremendously increase our ability to observe CBL depth routinely.

The dual-polarization upgrade to the 10-cm wavelength (S band) WSR-88D radars was completed in the United States in 2013, and with their installment came a wealth of untapped information (Kumjian 2013). With 160 locations covering much of the CONUS (NEXRAD Radar Operations Center 2023), and with routine scanning of the atmosphere every 5-10 min, WSR-88D radar observations provide high temporal and spatial resolution observations of the boundary layer. Differential reflectivity  $Z_{DR}$ , a dual-polarization radar variable available from WSR-88D radars, provides information about the shape and/or orientation of scatterers (Seliga and Bringi 1976) by taking the difference between the horizontally and vertically polarized reflectivity returns (in dB scale). Scatterers that are small compared to the radar wavelength with their mass oriented primarily horizontally produce positive  $Z_{DR}$  values, whereas those with their mass oriented primarily vertically produce negative values. Scatterers that have mass equally distributed horizontally and vertically, and/or have

random orientations, produce  $Z_{DR}$  values near 0 dB. Biota (insects and birds) tend to be nonspherical and oriented horizontally and are common in the CBL and just above it, producing  $Z_{DR}$ values of 2-6 dB. Bragg scattering-constructive interference of the backscattered electromagnetic waves caused by isotropic small-scale turbulence that mixes air with different refractive indices at scales half the radar wavelength and leads to  $Z_{DR}$  values near 0 dB (Doviak and Zrnić 1993; Melnikov et al. 2011)—is often present at CBL top. When combined with the scatter from biota, Bragg scattering produces a local minimum in  $Z_{DR}$  at the CBL top and values of the copolar correlation coefficient ( $\rho_{hv}$ ) between horizontally and vertically polarized signals near 1 (Melnikov et al. 2011). Using this information, Banghoff et al. (2018) manually estimated CBL depth from  $Z_{DR}$  signals in central Oklahoma for calendar year 2014 and compared them with nearby 0000 UTC rawinsonde-derived CBL depths. Results indicate that the CBL depths estimated from the WSR-88Ds and rawinsondes had a correlation of 0.90 and an RSME of only 254 m, with CBL depths varying from 200 to 3000 m over the 1-vr period. Banghoff et al. (2018) clearly demonstrate the ability of dual-polarization WSR-88D radar data to estimate CBL depth and suggest that this approach could be applied to observations from all WSR-88D radars.

The goal of this study is to develop an algorithm to automatically detect the CBL depth from WSR-88D radar  $Z_{\rm DR}$  observations. Section 2 discusses the data and methods used in this study, and section 3 provides details of the CBL depth algorithm, including a few simple quality control procedures. Results from the CBL depth calculations and quality control process are summarized in section 4, with conclusions in section 5.

#### 2. Data and methods

The main data source for this study is observations from the National Weather Service's dual-polarization WSR-88D radars. The radars operate with several different volume coverage patterns (VCPs) comprising a set of constant-elevation-angle surveillance scans completed every 4–10 min. During clear-air conditions when no precipitation signals are expected, data are collected roughly every 10 min from elevation angles between 0.5° and 4.5°; these are the primary observations used in this study. For other VCPs, the observations are collected more frequently; the time between volume scans depends upon the VCP selected, such that 10 min is the longest time interval between successive volume scans. The first WSR-88D range gate is from 2000 to 2250 m from the radar, with observations available every 250 m in range.

The  $Z_{\rm DR}$  observation is the key to sensing Bragg scatter and needs to be calibrated, which is accomplished routinely for the WSR-88D radar network by evaluating  $Z_{\rm DR}$  measurements for environmental conditions when  $Z_{\rm DR}$  should be near 0 (Zittel et al. 2014). One of these conditions is the clear-air return from Bragg scatter used in this study; other conditions include light rain and dry snow (Zittel et al. 2014; Richardson et al. 2017b). Calibration tests indicate that 60% of the WSR-88D radars have a system bias within  $\pm 0.2$  dB of 0 dB (Cunningham et al. 2013). Thankfully, even with some bias in the  $Z_{\rm DR}$  measurement, the

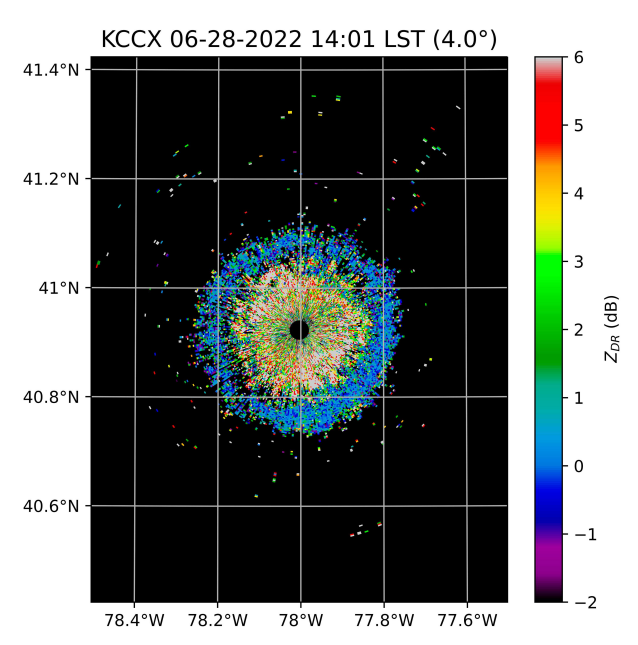


FIG. 1. Standard PPI scan of  $Z_{\rm DR}$  taken at 4° elevation angle at 1401 LST (+4 h for UTC) 28 Jun 2022 from the State College, PA, WSR-88D radar (KCCX) showing a blue ring of near-0-dB  $Z_{\rm DR}$  around the center of the radar indicative of Bragg scattering.

Bragg scatter signal for CBL top would still be identified as a local vertical minimum. The radar scan elevation angle also influences the  $Z_{\rm DR}$  value, but the influence is negligible for elevation angles less than 20° (Ryzhkov et al. 2016).

The constructive interference of the backscattered electromagnetic waves produced by Bragg scatter also creates a local enhancement of radar reflectivity factor Z at the CBL top (Doviak and Zrnić 1993; Melnikov et al. 2013). Unfortunately, the enhancement of Z from Bragg scatter often is overwhelmed in the CBL owing to signal contamination from biota (Heinselman et al. 2009; Melnikov et al. 2011, 2013), leading to Z not being helpful for observing CBL top.

When viewing  $Z_{\rm DR}$  observations within the CBL on a radar plan position indicator (PPI), the Bragg scatter layer at CBL top is discernable as a ring of local minimum in  $Z_{\rm DR}$  surrounding the radar site (Fig. 1) even when biota is present (Melnikov et al. 2011, 2013; Banghoff et al. 2018). The further the low- $Z_{\rm DR}$  ring is from the radar location (i.e., the center of a PPI scan), the higher in the atmosphere the scattering layer is located, providing information on the mean height of the Bragg scatter layer over this region. The height of this Bragg scatter layer is equivalent to the mean CBL depth above the radar site. CBL depths at other locations within the clear-air radar sampling umbrella can be determined by adding the difference in terrain height between the radar site and the desired location to the CBL depth.

To track the daytime evolution of CBL depth as indicated by a Bragg scatter layer, quasi-vertical profiles (QVPs) of  $Z_{\rm DR}$  are constructed from radar observations at each range gate averaged azimuthally over 360° (Kumjian et al. 2013; Ryzhkov et al. 2016) for the 4.5° elevation angle. This elevation angle is

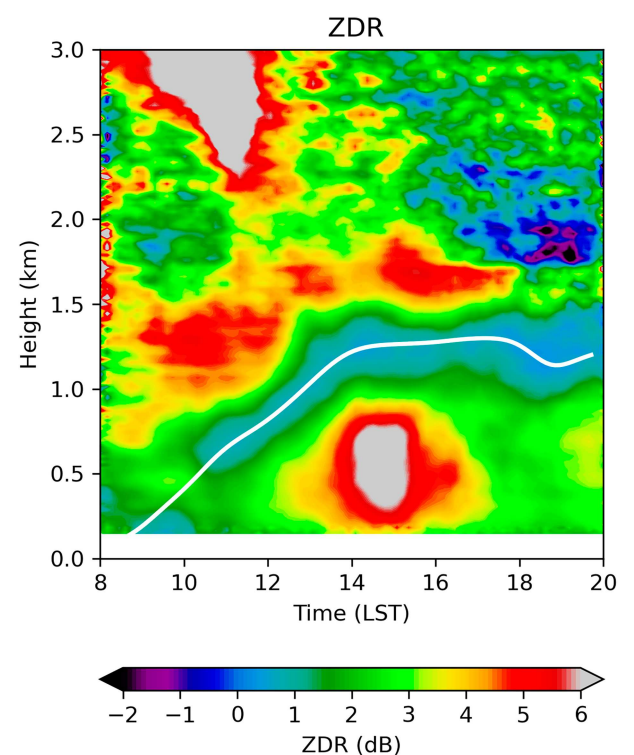


FIG. 2. QVP of  $Z_{\rm DR}$  from 3 Aug 2022 using observations from KCCX between 0800 and 2000 LST (1200 and 2400 UTC). The white line indicates the estimated top of the CBL, which tracks through a channel of local vertical minima in  $Z_{\rm DR}$ .

chosen to minimize the effects of ground clutter and is the highest elevation angle for clear-air sampling; if not available, then the first elevation angle  $\geq 4^{\circ}$  is used. Once the  $Z_{DR}$  observations are averaged azimuthally (in dB) for each range gate, range is converted to height AGL assuming standard atmospheric refraction (Doviak and Zrnić 1993), to create a vertical profile of the azimuthal mean  $Z_{DR}$  for a given volume scan and observation time. Since the center of the first range gate is located 2125 m from the radar, the lowest vertical observation in the QVP is 148 m AGL for the 4.5° elevation angle. Successive volume scans are combined to create a timeheight plot for each day from sunrise to sunset. Following Banghoff et al. (2018), the QVP of  $Z_{DR}$  is smoothed via a running mean over five time steps and three height levels to reduce noise in the QVPs for interpretability (Fig. 2). A QVP shows the temporal evolution of the vertical profile of radar observations and can be calculated for any radar variable or sample measure.

In an ideal situation, the QVP depicts a clear channel, or corridor, in which the azimuthal mean  $Z_{\rm DR}$  is a relative minimum (excluding negative values), starting near the ground a few hours after sunrise and rising to greater heights during the daytime hours. The center of this channel indicates the CBL top (Fig. 2, white line), where  $Z_{\rm DR}$  values are between 0 and 1 dB throughout most of the channel. Examination of thousands of daytime QVPs from across the WSR-88D network for two different years (2014 and 2022), however, shows

## KCCX 06-28-2022 QVPs

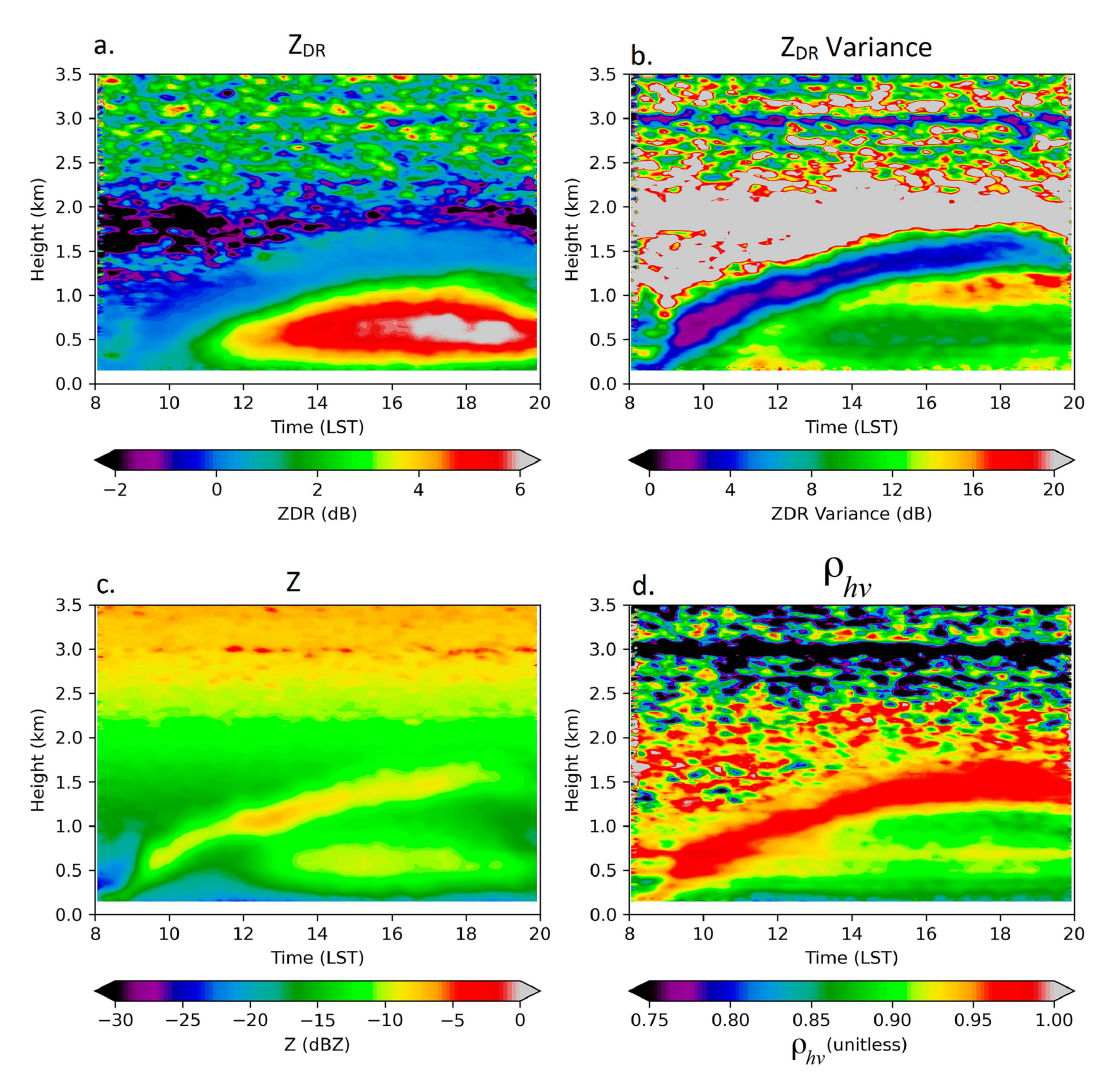


FIG. 3. QVPs of (a)  $Z_{\rm DR}$ , (b)  $Z_{\rm DR}$  variance, (c) Z, and (d)  $\rho_{\rm hv}$  from 0800 to 2000 LST (1200–2400 UTC) 28 Jun 2022 from KCCX. The CBL top reaches a depth of  $\sim$ 1.4 km by 1800 LST.

that this ideal situation is relatively rare. One common QVP type has  $Z_{\rm DR}$  values that decrease with height, perhaps with a weak vertical minimum, such that the  $Z_{\rm DR}$  channel is not obvious and is difficult to track (Fig. 3a). These uncapped QVPs led to the exploration of other radar variables that could assist in determining CBL top. As also shown in Heinselman et al. (2009), Melnikov et al. (2011, 2013), and Banghoff et al. (2018), a subjective analysis indicates clearly that while Z and  $\rho_{\rm hv}$  can be helpful in identifying CBL top in nearly ideal situations (Figs. 3c,d), these radar variables are unreliable for routinely identifying CBL top for most days. Thus,  $Z_{\rm DR}$  remains as the best dual-polarization radar variable for CBL top identification.

We hypothesize that, in addition to the central tendency as provided by the azimuthal mean  $Z_{\rm DR}$ , a measure of dispersion could provide additional information to help identify CBL top. In particular, the azimuthal variance of  $Z_{\rm DR}$  should have

a local minimum where  $Z_{\rm DR}$  is reduced from Bragg scattering, as Bragg scatterers should shift all the  $Z_{\rm DR}$  observations within the Bragg layer toward 0 dB. In addition, the  $Z_{DR}$  variance would likely increase above the CBL top as scatterers have lower concentrations and their  $Z_{DR}$  values become more variable. Visual inspection of thousands of QVPs confirms that azimuthal  $Z_{DR}$  variance is often just as helpful as  $Z_{DR}$  in identifying and tracking CBL top (Fig. 3b), as further confirmed by comparisons with QVPs of Z and  $\rho_{\rm hv}$  under ideal conditions. The two different  $Z_{\rm DR}$  sample measures often provide independent information as would be expected if the  $Z_{\rm DR}$  observations have a Gaussian distribution. Histograms of the azimuthal values of  $Z_{\rm DR}$  at constant range often show a Gaussian distribution within the CBL (not shown), although as the number of scatterers decreases above the CBL top, the distributions clearly are not Gaussian.

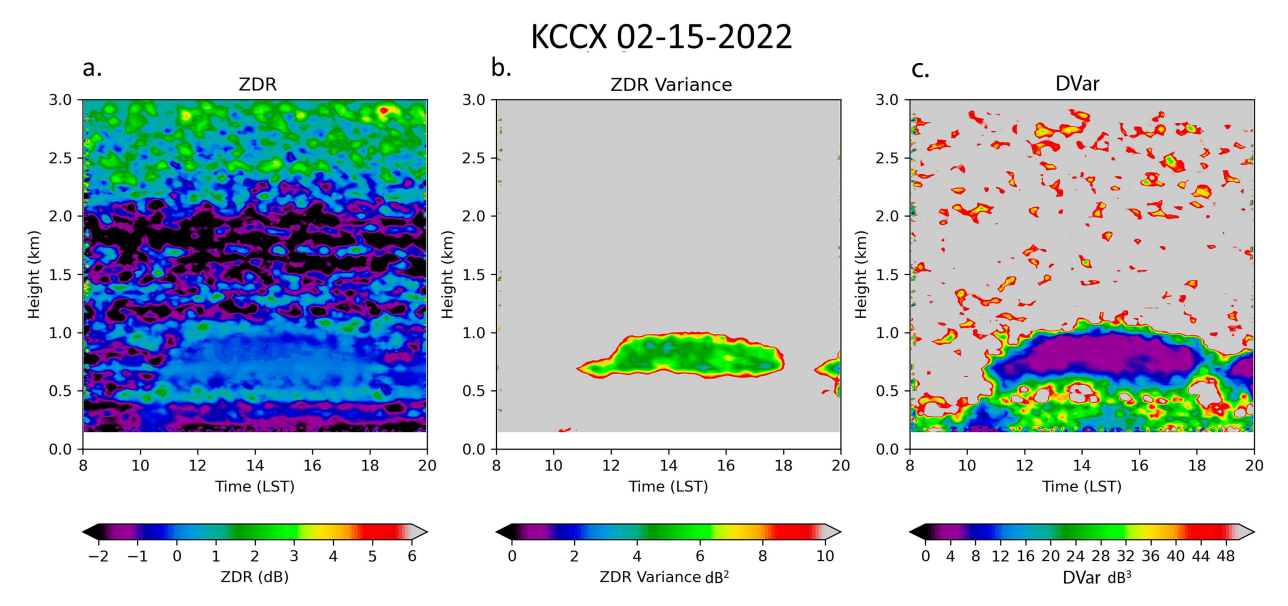


FIG. 4. Daytime QVP on 15 Feb 2022 from KCCX of (a)  $Z_{\rm DR}$ , (b)  $Z_{\rm DR}$  variance, and (c) DVar from 0800 to 2000 LST (1200–2400 UTC).

It is not unusual to find a local minimum of  $Z_{\rm DR}$  in regions of high  $Z_{\rm DR}$  variance, indicating that the low  $Z_{\rm DR}$  layer is unrelated to the Bragg scatter signal. To minimize the occurrence of this failure mode in the identification of CBL top, the two measures of the azimuthal  $Z_{\rm DR}$  distribution are combined to create a new variable DVar (units of dB³) with

DVar = 
$$(|\overline{Z_{DR}}| + 1) \left[ \frac{1}{n-1} \sum_{i=0}^{n} (Z_{DR_i} - \overline{Z_{DR}})^2 \right],$$
 (1)

where the overbar indicates the azimuthal mean, i represents the ith azimuth angle, and n is the number of azimuth angles in the elevation scan. The +1 dB is added to  $|\overline{Z_{\rm DR}}|$  so that DVar remains large when  $Z_{DR}$  variance is large, even when  $Z_{\rm DR}$  is small. On many days, detecting the CBL depth using DVar both reduces the noise in the  $Z_{DR}$  Bragg scatter signal and provides a means for detecting the CBL depth even in the occurrence of uncapped Bragg scatter signals. DVar homes in on the Z<sub>DR</sub> values near 0 dB that are relevant to Bragg scattering because the  $Z_{DR}$  variance within the Bragg scatter region is also reduced while the variance tends to be large outside of the channel. As a result, DVar retains values near 0 dB<sup>3</sup> within the Bragg scatter channel, with even larger values outside of the Bragg scatter channel, than seen with  $Z_{\rm DR}$  alone. This behavior is particularly helpful in identifying CBL top early in the daytime hours when a residual layer is present. A winter example for State College, Pennsylvania (KCCX), on 15 February 2022 (Fig. 4) demonstrates the use of DVar to locate the Bragg scatter region even though it is difficult to detect inspecting  $Z_{\rm DR}$  alone.

As can be seen from Figs. 2–4, the structures seen in the QVPs of  $Z_{\rm DR}$  are often complex and are influenced by more than just Bragg scattering at CBL top. Melnikov et al. (2013) and Melnikov and Zrnić (2017) discuss several additional atmospheric Bragg scatter signatures that can be detected from

 $Z_{\rm DR}$  observations, including nonprecipitating clouds and turbulent motions within strong vertical gradients in RH. Thus, it is not surprising that even when using DVar, there can be missed or inaccurate CBL depth identification, as radar observations of CBL and lower-atmospheric structures can be irregular and tracking a channel of noisy observations is difficult to automate. Herein, two separate methods for tracking the low- $Z_{\rm DR}$  channel are developed; the best results are found when results from both approaches are combined.

To evaluate the accuracy of the CBL depth algorithm, small rawinsondes called Windsonds are launched from the Pennsylvania State University campus in University Park, PA, to compare with the CBL depth estimated using WSR-88D radar observations from the State College (KCCX) radar located approximately 20 km to the northwest of campus. Windsonds are lightweight rawinsonde systems manufactured by Sparv Embedded that use a small helium balloon and provide standard measurements of atmospheric pressure, temperature, RH, and winds, with observations every second (typical rise rates of 2-3 m s<sup>-1</sup>, providing observations every 2-3 m), up to several kilometers above ground level (AGL). Windsond observations compare favorably to a commonly used rawinsonde system (Bessardon et al. 2019), and the sondes have been used as pseudo-Lagrangian drifters to study convective storms by Markowski et al. (2018) and Bartos et al. (2022). Following Banghoff et al. (2018), values of the atmospheric refractive index for S-band radiation, converted to refractivity N (e.g., Doviak and Zrnić 1993),  $\theta$ , and  $q_v$ , are calculated from the soundings and the heights with the maximum vertical gradients determined. Results from Seidel et al. (2010) suggest that mean CBL depths from these three variables selected differ by <250 m. Following Banghoff et al. (2018), the modal height among the three variables is used to determine CBL height and avoid outliers, and when multiple vertical gradient maxima are present, then the height of the lower maxima is used as the CBL depth

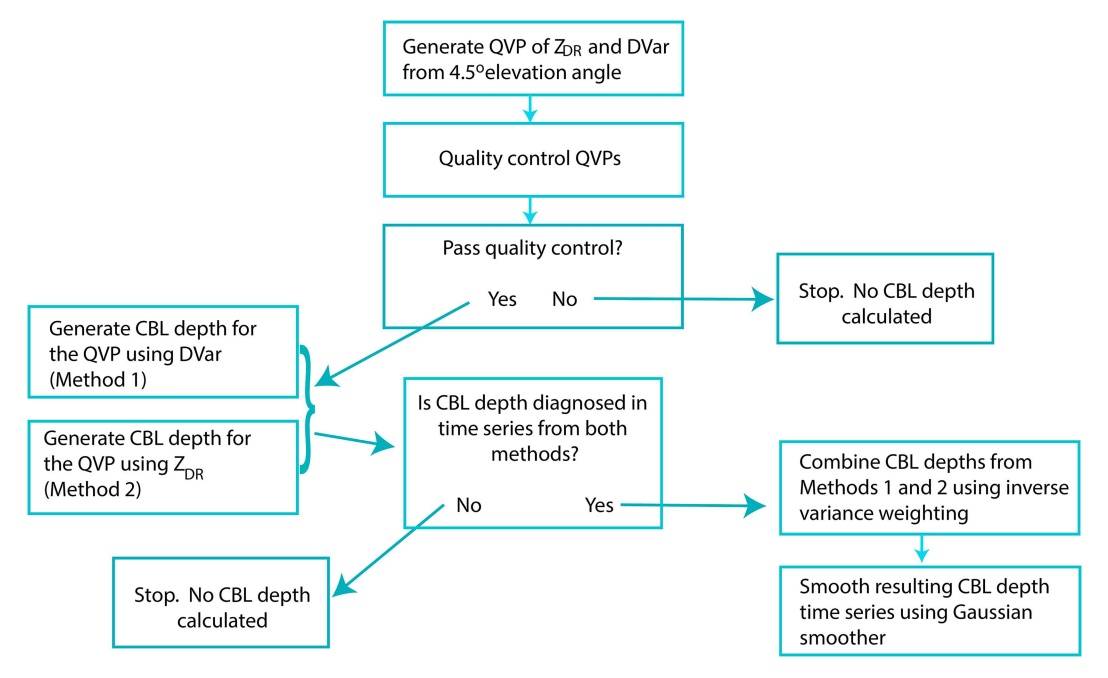


FIG. 5. Flowchart of the methodology used to determine CBL depth from the WSR-88D radars using Z<sub>DR</sub> observations.

estimate. The Windsond-determined CBL height is adjusted for the 381-m difference in terrain height between the radar station KCCX and the Windsond launch site.

#### 3. Algorithm to estimate CBL depth

QVPs of  $Z_{DR}$  and DVar are created between local sunrise and sunset at 50 selected WSR-88D radar locations spread across CONUS for each day during 2014 and 2022 to develop and assess the algorithm. These 2 years are chosen owing to contiguous U.S. rainfall total being 0.92 in. above the 1901-2000 mean in 2014 and 1.49 in. below the 100-yr mean in 2022, with different statewide rainfall distributions, allowing for the exploration of QVP behaviors under different environmental conditions (NCEI 2024). As each day is processed, a few quality control metrics are applied to the QVP to remove days where a CBL top signal is not expected. The presence of rain is diagnosed in the QVP using a combination of Z and  $\rho_{hv}$ . If Z > 10 dBZ and  $\rho_{hv} > 0.8$  for more than 2 h in succession over multiple heights, then rain is considered present and no CBL depth is calculated for the day (Banghoff et al. 2018). Light or frozen precipitation is diagnosed similarly when there are four consecutive volume scans where the value of DVar is <3 dB<sup>3</sup> (this threshold was determined experimentally) and CBL depth is not calculated for the day. Banghoff et al. (2018) applied a similar approach using  $Z_{DR}$  values < 2 dB for an entire column to identify light precipitation. However, we found this approach to be inadequate at many stations, particularly in winter, resulting in a high rate of false detection of light precipitation. CBL depth also is not calculated for the day when the radar is offline for >1 h during the daytime hours.

Out of the total 35 105 QVPs created for these 2 years of radar observations, 8792 (25%) were removed due to rain, 541 (1.54%) were removed due to light/frozen precipitation, and 1435 (4.09%) were removed due to the radar being down. CBL depth is estimated for every volume scan from the remaining 24337 QVPs. As the final quality control step, and prior to processing the radar observations to compute the CBL depth, each QVP is inspected manually to see if there is a visible signal of the  $Z_{\rm DR}$  channel indicating the CBL top is detectable. A flowchart showing the steps taken to determine CBL depth from the QVPs is shown in Fig. 5.

#### a. Method 1: Continuous vertical minimum in DVar

The first method developed to identify CBL depth is based on a QVP of DVar. The method begins by analyzing the vertical DVar profiles 2.5–3.5 h after sunrise to identify the first local minimum of DVar situated above the ground. By this time, solar heating should be warming the ground and the CBL should be deepening (Angevine 2008). Prior to locating the first local minimum in DVar, the CBL depth is set to 0 m to avoid the detection of residual layers. Unless there are data missing in this time window, an initial minimum is always detected.

Once the initial local vertical minimum in DVar is found, the algorithm searches for a local minimum within the next volume scan at a higher height, as it is assumed that the CBL depth does not decrease during the early daytime hours. Through trial-and-error testing, maximum growth rates are used to constrain the CBL depth growth rate, with the values set based on the season. For April through October, the maximum growth rate of CBL depth is set to 0.25 m s<sup>-1</sup> (900 m h<sup>-1</sup>), a value based on observations, whereas for the remaining months,

#### KCCX 06-28-2022

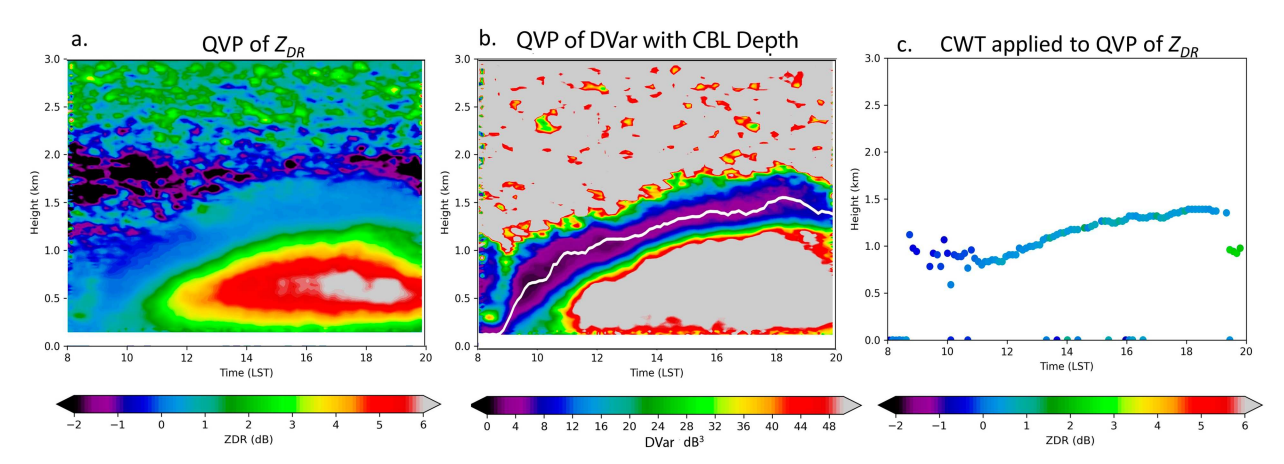


FIG. 6. Daytime (a) QVP of  $Z_{\rm DR}$ , (b) QVP of DVar used in method 1, and (c) local minima in  $Z_{\rm DR}$  detected by the CWT used in method 2. The white line in (b) indicates the CBL depth estimated from method 1. The QVP is from radar observations at State College, PA (KCCX), from 0800 to 2000 LST (1200–2400 UTC) 28 Jun 2022.

it is set to 0.14 m s<sup>-1</sup> (500 m h<sup>-1</sup>). To also allow the CBL depth to decrease in the afternoon, a minimum growth rate is set to -0.055 m s<sup>-1</sup> (-200 m h<sup>-1</sup>) for all months and applied starting 3 h before sunset. The time increments between radar volume scans are used to determine the maximum depth increase/decrease from one volume scan to the next. After the first 3 h, the CBL height is allowed to either increase or remain steady while searching for the CBL depth based on DVar minima within the growth rate constraints. The algorithm yields estimated CBL depths at every volume scan from sunrise to sunset (Fig. 6b). Visual inspection of the results suggest that this method is particularly good at identifying the low DVar channel in the morning hours into the early afternoon, but occasionally runs into difficulties late in the afternoon when the channel can become very deep.

## b. Method 2: Continuous wavelet transform applied to $Z_{DR}$

The second method developed to identify CBL depth uses the QVP of  $Z_{DR}$  and a local continuous wavelet transform (CWT) to identify the local minima in  $Z_{DR}$  within each volume scan. As the name suggests, a local CWT provides information related to the local behavior and characteristics contained within the signal (Gamage and Hagelberg 1993). The CWT is performed on a vector of interest; in this case, the vector is the vertical profile of  $Z_{\rm DR}$  at a given time. The CWT produces a collection of coefficients that contain information about the strength of the relationship between the wavelet and the signal. The only specification required is a range of peak widths describing the desired scale of the wavelet function to be applied. The CWT method has been used in the study of many meteorological phenomena ranging from El Niño-Southern Oscillation to cold fronts (Torrence and Compo 1998) as well as CBL depth detection using lidar and wind profilers (Brooks 2003; Compton et al. 2013). A major

benefit of a CWT is that it can be used directly on raw data without any prior filtering or baseline removal (Du et al. 2006) and is easily repeatable, making it a desirable technique for locating minima in QVPs of  $Z_{\rm DR}$ . However, results suggest that some filtering is beneficial prior to applying the CWT. First, values of  $Z_{\rm DR} < -0.75$  dB are set to missing since any large negative  $Z_{\rm DR}$  values are not indicative of Bragg scattering (Melnikov et al. 2011). Second, the mean  $Z_{\rm DR}$  and its standard deviation are calculated from observations within the entire PPI scan, and values of  $Z_{\rm DR}$  greater than the mean plus one standard deviation in a scan are removed to limit peak detection of local minima found in areas of high  $Z_{\rm DR}$ .

For this study, a CWT with a Ricker wavelet is used to find the local minima of  $Z_{\rm DR}$  in QVPs (Fig. 7). Ricker wavelets are designed for finding localized maxima or minima in a

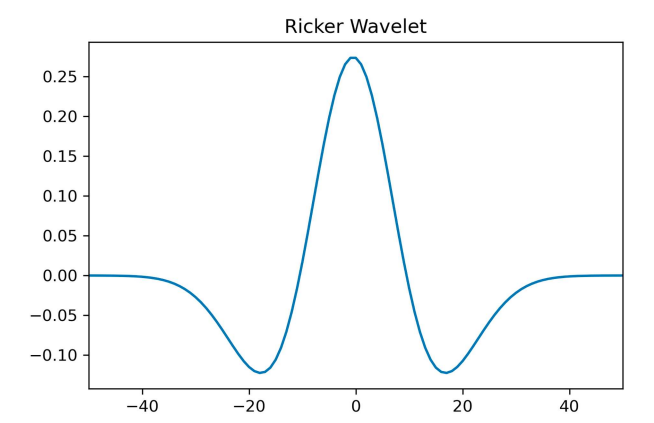


FIG. 7. Example of a Ricker wavelet with peak width a=10, with wavelet amplitude on the y axis and data levels on the x axis. Larger values of peak widths produce wavelets with larger spatial scale.

signal owing to its own sharp peak. The CWT equations for the Ricker wavelet are as follows (Daubechies 1992; Ryan et al. 1994):

$$C(a, b) = \int s(l)\psi_{a,b}(l) dl, \qquad (2)$$

$$\psi_{a,b}(l) = \frac{1}{\sqrt{a}} \psi \left( \frac{l-b}{a} \right), \tag{3}$$

$$\psi(x) = 1 - (2\pi^2 f^2 x^2) e^{(-\pi^2 f^2 x^2)},\tag{4}$$

where C is the 2D matrix of wavelet coefficients, s(l) is the vector signal (in this study, the vertical profile of  $Z_{\rm DR}$  for a given time),  $\psi_{a,b}(l)$  is the scaled and translated wavelet, a is the scaling term (i.e., the specified peak widths ranging from 1 to 10 in the morning and from 1 to 30 for the afternoon hours), l is the vertical level of the  $Z_{\rm DR}$  observations, b is the vertical level of the wavelet center,  $\psi(x)$  is the mother wavelet (the Ricker wavelet), and  $f = 2\pi/a$  is the wavenumber. The wavelet coefficients reflect the strength of the pattern matching between the signal and  $\psi_{a,b}(l)$ , with larger coefficient values indicating stronger matching.

Once the CWT matrix is calculated, peak detection is applied on the data using the approach of Du et al. (2006). The local maximum of the CWT coefficients at each scale is found, as these are correlated with local minima in  $Z_{\rm DR}$ . Ridgelines are created at the levels of the local maxima in the CWT coefficients, and the CWT coefficients are used to determine the signal-to-noise ratio (SNR; Du et al. 2006). From the SNR and detected ridges, the algorithm finally identifies the true minima in the  $Z_{\rm DR}$  signal. By determining SNR in the wavelet space, rather than the signal space, this method removes the need for baseline correction and other data filtering (Du et al. 2006).

As in method 1, the CBL depth is set to the lowest local minima detected by the CWT if it is found below 250 m within the first 3.5 h after sunrise and set to 0 m if there are no minima detected below 250 m. The maximum and minimum growth rates between consecutive points are set to the same values as those used in method 1. The algorithm yields estimated CBL depths for every volume scan from sunrise to sunset. If the CWT approach fails to identify a CBL depth for a single volume scan, then linear interpolation is applied to fill the gap. If the CWT approach fails to identify a CBL depth for two successive volume scans, then the CWT approach ends and no CBL depth is determined for the day.

An example of the Ricker CWT method applied to a QVP of  $Z_{\rm DR}$  is shown in Fig. 6c. Each point represents a local minimum in  $Z_{\rm DR}$  found in the QVP by the Ricker CWT using peak widths a from 1 to 10 in the morning and from 1 to 30 in the afternoon and evening. The range of peak widths tells the CWT how significant the minima must be to be detected. Larger peak widths mean that the CWT only detects very noticeable, broader minima, while smaller peak widths mean that the CWT finds many smaller-scale local minima. Peak width is related to the data interval, which is about 20 m for the QVP. Thus, peak widths a = 1–10 are used in the morning because the peaks in the  $Z_{\rm DR}$  signals at those times have

smaller scale. During the afternoon hours, however, the CWT need only locates the major minima in the  $Z_{\rm DR}$  signal. Visual inspection of many QVPs suggests that method 2 works particularly well late in the afternoon when wide channels are often observed in the QVP.

#### c. Combined algorithm

The two CBL depth estimates determined from methods 1 and 2 are combined using an inverse variance weighting approach. Since method 2 uses values of  $Z_{\rm DR}$  only to calculate CBL depth, the observed root-mean-square error of  $\sigma_2=250$  m from Banghoff et al. (2018) is used as the variance for this method. The variance for method 1 that uses DVar to calculate CBL depth is determined after extensive subjective comparisons against observed  $Z_{\rm DR}$  channels. The best results are found using  $\sigma_1=175$  m. The CBL depth estimates from method 1  $(h_1)$  and method 2  $(h_2)$  are then combined to calculate the CBL depth h at each observation time using

$$h = \frac{\sigma_2^2 h_1 + \sigma_1^2 h_2}{\sigma_1^2 + \sigma_2^2}.$$
 (5)

Since  $\sigma_1 < \sigma_2$ , the CBL depth estimate from method 1 receives more weight than the CBL depth estimate from method 2. This weighting is particularly helpful during the early daytime hours when DVar captures the initial growth of the CBL.

Once the variance-weighted CBL depth for a single time is determined, the algorithm repeats for the volume scan at the next time. After the inverse variance weighting method has been applied over all times, the result is smoothed separately in time using one application of a 1D Gaussian filter:

$$G(l) = \frac{1}{\sqrt{2\pi\sigma^2}} e^{-(l-m)^2/(2\sigma^2)},\tag{6}$$

in which l and m are the time intervals and  $\sigma = 4$  time units.

After applying the inverse variance weighting and Gaussian smoothing, the result is a time series of CBL depths for the selected day. The result of the combined algorithm using the CWT minima and DVar for observations at KCCX on 28 June 2022 demonstrates the ability of the algorithm to detect CBL depth even when the top of the CBL is not clearly bounded by scatterers from above (Fig. 8). This is one of the merits of including  $Z_{\rm DR}$  variance, as biota are not always present above the CBL to scatter significant radiation, particularly in winter. In these instances, the  $Z_{\rm DR}$  variance is noticeably lower in the region of Bragg scatter than the area above and below and helps identify the CBL top.

### 4. Algorithm results

Comparisons of the CBL depths estimated from the algorithm with Windsond measurements collected on selected days at State College, Pennsylvania, during 2022 show very good agreement (Fig. 9). On 28 June 2022, the evolution of the CBL as determined by the algorithm shows that the CBL begins to deepen shortly after 0800 LST (Fig. 9a) and grows

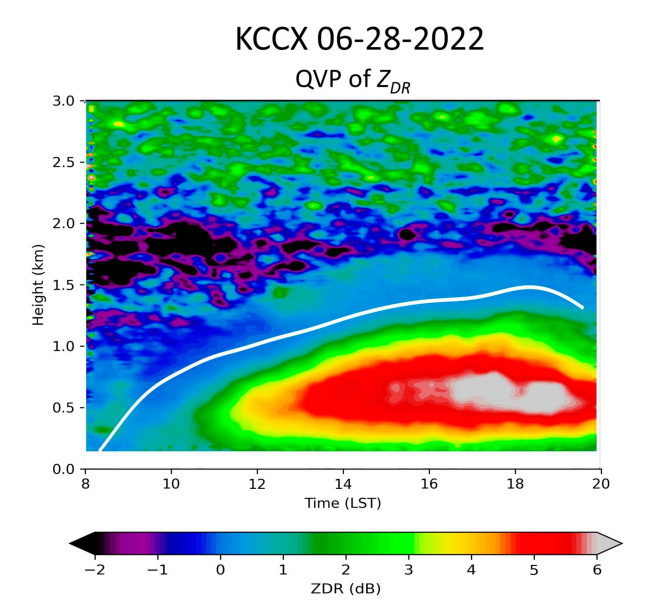


FIG. 8. Daytime QVP of  $Z_{\rm DR}$  with the white line indicating the computed CBL depth from combined methods 1 and 2 from radar observations at State College, PA (KCCX), from 0800 to 2000 LST (1200–2400 UTC) 28 Jun 2022.

sharply over the next few hours before levelling off to a more gradual increase in depth during the afternoon. After reaching its peak at 1800 LST, the CBL depth begins to decrease in the evening. During this day, four Windsonds were launched at 1006, 1159, 1358, and 1555 LST. The CBL depth diagnosed from the first three soundings shows that the CBL depth algorithm values are within 100 m of the CBL depths from rawinsondes; for the last sounding, the rawinsonde CBL depth is 200 m greater than the value from the algorithm.

On 3 August 2022, the channel of low  $Z_{\rm DR}$  values from KCCX is much thinner and bounded by scattering from biota above and below (Fig. 9b). The growth of the CBL after sunrise begins linearly and continues until near 1400 LST when the CBL depth remains nearly steady for a few hours. The CBL depth then decreases around 1730 LST before increasing slightly again at 1900 LST. The diagnosed CBL depth from Windsond launches at 1226, 1354, and 1520 LST all fall within 100 m of the values from the CBL depth algorithm.

An even thinner Bragg scatter channel is seen from KCCX on 15 September 2022 (Fig. 9c), with the CBL slowly deepening through the day before decreasing beginning at 1700 LST. CBL depths diagnosed from the Windsond launches at 1134 and 1301 LST align well with those from the CBL depth algorithm: the 1134 LST Windsond-derived CBL depth is <50 m below the algorithm's computed CBL depth and the 1301 LST Windsond-derived CBL depth is <100 m above the algorithm's computed CBL depth.

Last, a QVP typical of the late fall and winter months with  $Z_{\rm DR} < 3$  dB throughout the day occurs on 8 November 2022 at KCCX (Fig. 9d). Despite the small  $Z_{\rm DR}$  values, there is still a visible signal in the QVP that identifies the CBL top, which increases from 1000 to 1600 LST before decreasing after

1600 LST. The Windsond launches at 1337 and 1433 LST both lie nearly on the algorithm-computed CBL depth, with differences of  $<\!15$  m. This suggests that the CBL depth algorithm successfully detects the CBL depth from WSR-88D QVPs of  $Z_{\rm DR}$  data.

Using the observations collected from 43 Windsond launches during 2022, the CBL depth algorithm applied at KCCX radar had a mean error (bias) of -36 m and an RMSE of 148 m. The RMSE of 148 m is less than the RMSE of 254 m calculated by Banghoff et al. (2018) when manually estimating CBL depth from  $Z_{\rm DR}$  observations and comparing with nearby rawinsondes.

We visually inspected thousands of  $Z_{DR}$  QVPs to ascertain if the algorithm placed the CBL depth within a visible low-Z<sub>DR</sub> or low-DVar layer that had a characteristic CBL evolution. With complex  $Z_{DR}$  and DVar structures within the QVPs and no verifying observations, the actual CBL depth on these days is unknown—we can only evaluate whether the CBL depth algorithm yielded a reasonable path through the low  $Z_{\mathrm{DR}}$  and DVar layers. To provide more context for this subjective analysis, the CBL depth algorithm results are shown for a variety of days and WSR-88D radars, with estimated maximum CBL depths ranging between 1 and 2.5 km (Fig. 10). The  $Z_{\rm DR}$  channels are apparent on each day, but the structure and complexity of the  $Z_{DR}$  fields vary. Overall, the CBL depth algorithm is highly effective at locating the visible  $Z_{\rm DR}$  minima and capturing the growth of the CBL throughout the day. The CBL for KLRX (Elko, Nevada) on 4 May 2022 grows sharply after sunrise and then transitions to constant depth after 1200 LST (Fig. 10a), with the algorithm-computed CBL following exactly where the minimum in  $Z_{DR}$  lies. The QVP for KYUX (Yuma, Arizona) on 9 June 2014 shows a Bragg scatter layer that is less defined, but still present (Fig. 10b), with the CBL growing rapidly from 0800 to 1300 LST and decreasing in depth after 1530 LST. For KAMA (Amarillo, Texas) on 10 June 2022, the CBL top is very clear in the beginning of the day, from 0800 to 1300 LST, before the signal is contaminated by large  $Z_{\rm DR}$  values (Fig. 10c). Despite this signal contamination, the CBL depth algorithm interpolates the approximate location of the CBL top using local minima of  $Z_{DR}$  and DVar. The QVP from KGRK (Fort Worth, Texas) on 3 January 2014 shows a CBL case for a winter day (Fig. 10d). Inspection of many QVPs in winter indicates that the  $Z_{\rm DR}$  values are reduced due to the lack of biological scatterers in the atmosphere, yet the CBL depth algorithm still tracks the channel. On 5 July 2022, the KAMA QVP (Fig. 10e) shows a very high CBL top, which increases steeply from the morning through the late afternoon. In this case, evening rain develops. Last, observations from KYUX on 10 May 2014 (Fig. 10f) show the development of a Bragg scatter layer that begins as a narrow channel and then becomes unbounded at the top. For all six of these cases, the CBL depth algorithm performed well, showing promise for its application to a wide range of days and locations. Manual inspection of thousands of QVPs with overlaid CBL depth algorithm results yield a similar conclusion, and subjectively, we estimate that the CBL depth algorithm calculates a reasonable depth that fits within the  $Z_{\rm DR}$  signal channel more than 95% of the time.

Note that CBL depth estimation from dual-polarization radars is impossible when it rains, since raindrops also yield low  $Z_{DR}$  values and produce large  $Z_H$  that overwhelms any signal

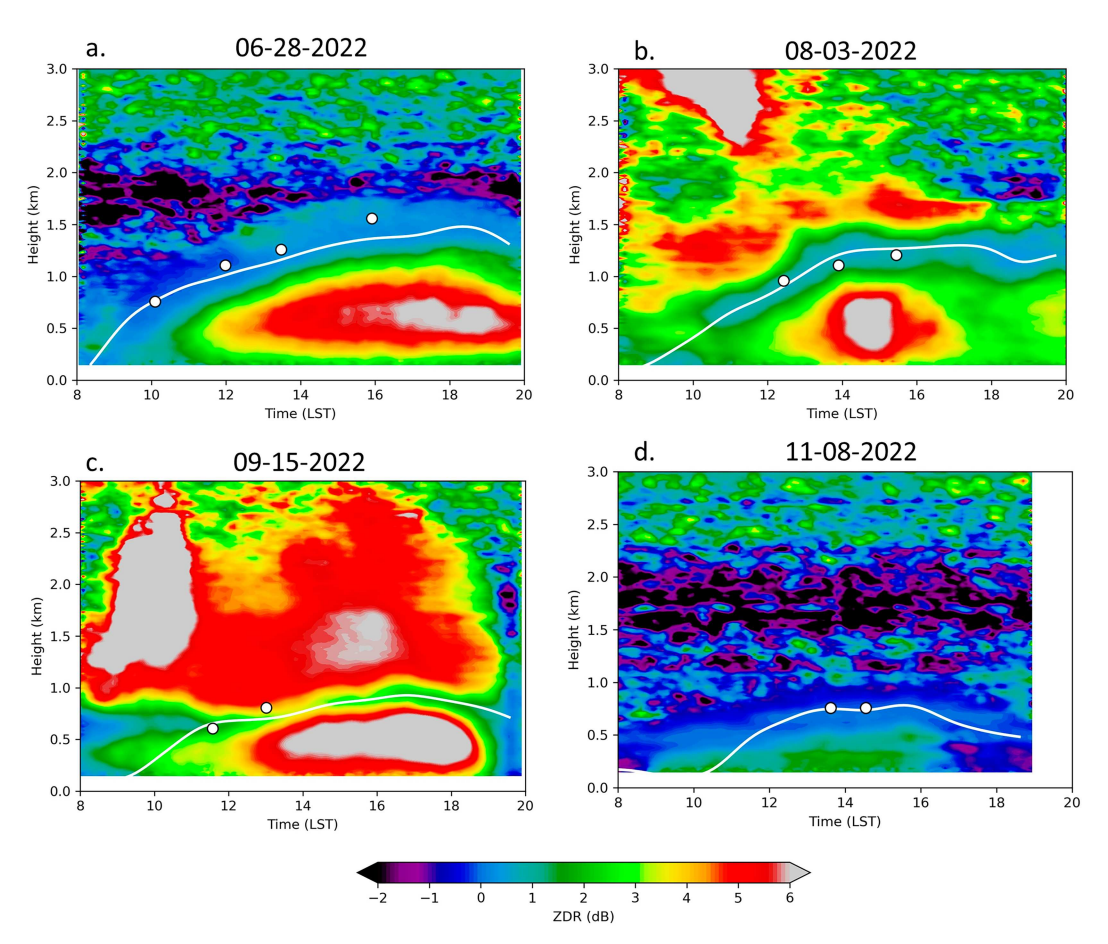


FIG. 9. QVPs of  $Z_{\rm DR}$  with the CBL depth algorithm calculated CBL depth (white line) and Windsond-diagnosed CBL depth (white circle) for KCCX on (a) 28 Jun 2022, (b) 3 Aug 2022, (c) 15 Sep 2022, and (d) 8 Nov 2022 from 0800 to 2000 LST (1200–2400 UTC).

from Bragg scattering, thereby rendering it useless for CBL detection. Additionally, chaff also creates problems for radar locations near military bases (Zrnić and Ryzhkov 2004). Finally, applying this algorithm within regions of complex terrain introduces additional challenges, as mountains can interrupt radar beams, creating missing azimuths in the datasets that complicate the identification of the CBL top signature.

Two distinct CBL growth modes are suggested in many of the QVPs. In the first and most common mode, the low DVar layer (and low  $Z_{\rm DR}$  layer, not shown) takes on a characteristic S shape, as seen in a QVP from Sterling, Virginia (KLWX; Fig. 11a), in which the CBL deepens slowly for a few hours, then deepens much quicker until it reaches a maximum depth, and stays at a nearly constant value until sunset. The Sterling, Virginia, 0800 LST (1200 UTC) sounding (Fig. 11b) shows a shallow stable layer and a residual layer that extends upward to near 800 hPa ( $\sim$ 1.9 km AGL) with a strong capping inversion on top. The 2-m temperatures observed near Sterling first become warm enough for undiluted surface parcels ascending along a dry adiabat to remain positively buoyant and rise through the residual layer sometime between 1000 and 1100 LST (1400 and 1500 UTC). This time interval corresponds to when the low

DVar layer is rising quickly in the QVP (Fig. 11a). Maximum 2-m temperatures reach 27°C and are not warm enough for the CBL to grow above the strong capping inversion. The 2000 LST (2400 UTC) evening sounding from Sterling (not shown) indicates a CBL depth between 1.5 and 2 km, in good agreement with the low DVar layer in the QVP at this time. Analyses of soundings from other days suggest that the S-shaped CBL growth mode occurs when the CBL entrains a residual layer from the previous day and does not deepen much further.

The second distinct QVP growth mode has the low DVar layer deepening consistently with time throughout the day, as again as seen in a QVP from KLWX (Fig. 12a). For this case, the 0800 LST Sterling sounding shows a shallow stable layer, with an 800-m deep residual layer above and a weak capping inversion (Fig. 12b). As the surface warms, the CBL depth increases quickly, the residual layer is entrained into the CBL, and the CBL continues to deepen into and above the capping inversion as the ground surface continues to warm. Maximum 2-m temperatures near Sterling reach 27°C; assuming a well-mixed CBL, an undiluted surface parcel would become neutrally buoyant just above 800 hPa. The 2000 LST (2400 UTC) sounding from Sterling indicates a CBL depth of approximately

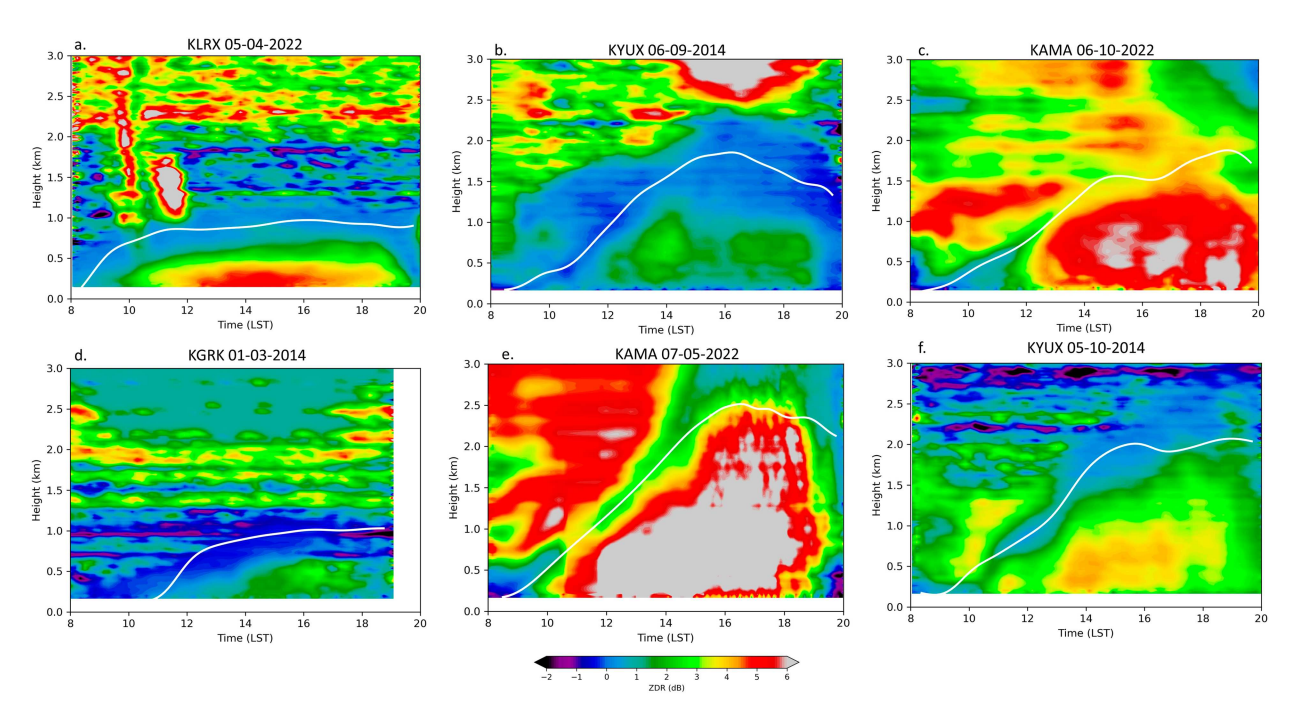


FIG. 10. QVPs of  $Z_{\rm DR}$  for (a) KLRX (Pacific station) 4 May 2022, (b) KYUX (mountain station) 9 Jun 2014, (c) KAMA (central station) 10 Jun 2022, (d) KGRK (central station) 3 Jan 2014, (e) KAMA 5 Jul 2022, and (f) KYUX 10 May 2014. All times are LST. The white lines are the CBL depths determined by the algorithm.

2.5 km AGL (not shown), in good agreement with the low DVar layer in the QVP at this time. Thus, this CBL growth mode occurs when the CBL deepens to well above the top of the residual layer (if any) present in the morning sounding, as can occur after cold frontal passage. Similar CBL growth modes are suggested in the range-corrected boundary layer profiler signal-to-noise ratio time–height plots in Angevine et al. (1994).

#### 5. Conclusions

We developed an algorithm to estimate CBL depth from QVPs of  $Z_{\rm DR}$  and DVar using observations from dual-polarization WSR-88D radars. Two methods to compute CBL depth are

developed and combined using an inverse-variance weighting approach to yield the best results across a variety of QVP structures. Comparisons of the calculated CBL depth from the KCCX radar against nearby Windsond observations yield a CBL depth RMSE of 148 m; this RMSE is below the RMSE range for CBL depth estimation algorithms from wind profilers ranging from 152 to 424 m and very close to the RMSE of CBL depth estimation among experts (109–135 m; Bianco et al. 2008). Subjective assessments suggest that the algorithm can accurately handle a variety of complex QVP structures to arrive at reasonable CBL depths based on our understanding of QVPs of  $Z_{\rm DR}$ . Winter months prove to be the most difficult due to the lack of biological scatterers in

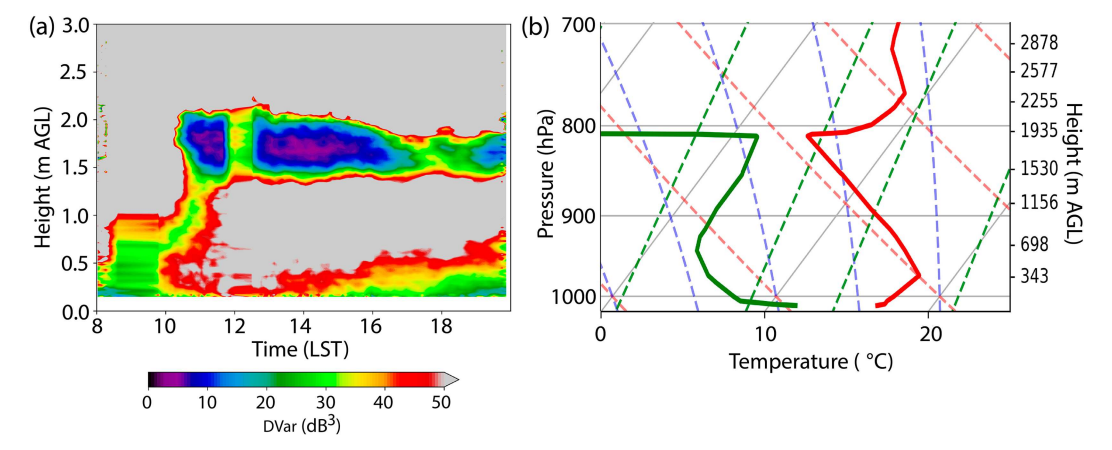


Fig. 11. (a) QVP of DVar at KLWX (Sterling, VA) from 0800 to 2000 LST (1200–2400 UTC) and (b) the Sterling, VA, rawinsonde launch at 0800 LST (1200 UTC) 28 Jun 2022.

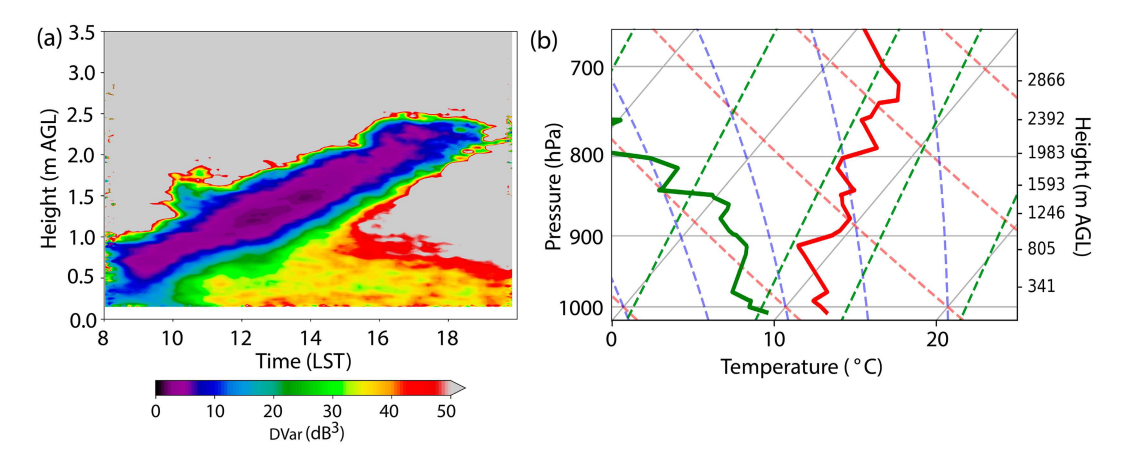


FIG. 12. (a) QVP of DVar at KLWX (Sterling, VA) from 0800 to 2000 LST (1200–2400 UTC) and (b) the Sterling, VA, rawinsonde launch at 0800 LST (1200 UTC) 21 May 2023.

the atmosphere and a decreased moisture gradient at the top of the CBL, which contribute to fewer identifiable CBL top signals in the QVPs.

The ability of WSR-88D  $Z_{\rm DR}$  observations to detect CBL depth is clear, although there will always be days in which the CBL depth signature is overwhelmed by falling precipitation or is otherwise unidentifiable. There also can be horizontal variations in CBL depth, as produced by sea breezes, lake breezes, convective outflows, or frontal zones, which could influence the calculation. Exploration of several months of observations from WSR-88Ds near coastal regions indicates that sea breezes have only a minor impact on the estimated CBL depth, although further study is warranted. The potential value of an automated CBL depth algorithm from radar in operations is significant, as such an approach could provide reasonable estimates of CBL depth at any given radar location with a 5-10-min temporal resolution and thereby assist daily forecasts of air pollution and convection initiation. Modeling efforts also could benefit from frequent estimates of CBL depth, providing key verification information to improve PBL parameterization schemes without increased rawinsonde launches. The implementation of automated CBL depth estimation from radar could revolutionize our observations of CBL depth without added costs of new instruments and could lead to improvements in modeling CBL structure and its impact on weather.

To further automate the process of identifying the CBL height in QVPs, artificial intelligence could be used to identify the QVPs with a detectable Bragg scatter signal rather than the methods developed here. It also would be helpful to quality control the estimated CBL depth based on the WSR-88D observations, such that days when the CBL depth cannot be accurately estimated are identified easily in real time. Finally, the unique terrain and vegetation characteristics of the WSR-88D sites suggest that some tuning of the adjustable parameters (i.e., maximum and minimum growth rates) would likely improve results.

Acknowledgments. Funding for this research was provided by the National Science Foundation under Award AGS-2045504. Special thanks to Sonya Lewis for assisting

with QVP generation and quality control, to Cynthia Simon and Fabiola Guillaume for exploring QVPs in coastal regions as part of a Research Experience for Teachers program, and to two anonymous reviewers for their helpful and constructive comments. Windsonds are from Sparv Embedded. This work is part of the first author's master's thesis at The Pennsylvania State University. Any opinions, findings, and conclusions or recommendations expressed in this publication are those of the authors and do not necessarily reflect the views of the National Science Foundation.

Data availability statement. WSR-88D observations used in this study are freely available from the National Center for Environmental Information (NCEI) and Amazon Web Services. Windsond observations collected at Penn State are available via the Penn State Data Commons at https://doi.org/10.26208/5NN6-KV44 (Stouffer et al. 2024).

#### REFERENCES

Angevine, W. M., 2008: Transitional, entraining, cloudy, and coastal boundary layers. *Acta Geophys.*, 56, 2–20, https://doi. org/10.2478/s11600-007-0035-1.

—, A. B. White, and S. K. Avery, 1994: Boundary-layer depth and entrainment zone characterization with a boundary-layer profiler. *Bound.-Layer Meteor.*, 68, 375–385, https://doi.org/ 10.1007/BF00706797.

Banghoff, J. R., D. J. Stensrud, and M. R. Kumjian, 2018: Convective boundary layer depth estimation from S-band dual-polarization radar. J. Atmos. Oceanic Technol., 35, 1723–1733, https://doi.org/ 10.1175/JTECH-D-17-0210.1.

Bartos, E. A., P. M. Markowski, and Y. P. Richardson, 2022: Three-dimensional thermodynamic observations in supercell thunderstorms from swarms of balloon-borne sondes. *Mon. Wea. Rev.*, 150, 1689–1723, https://doi.org/10.1175/MWR-D-21-0122.1.

Bessardon, G. E. Q., K. Fosu-Amankwah, A. Petersson, and B. J. Brooks, 2019: Evaluation of Windsond S1H2 performance in Kumasi during the 2016 DACCIWA field campaign. *Atmos. Meas. Tech.*, 12, 1311–1324, https://doi.org/10.5194/amt-12-1311-2019.

- Bianco, L., J. M. Wilczak, and A. B. White, 2008: Convective boundary layer depth estimation from wind profilers: Statistical comparison between an automated algorithm and expert estimations. *J. Atmos. Oceanic Technol.*, 25, 1397–1413, https:// doi.org/10.1175/2008JTECHA981.1.
- Bright, D. R., and S. L. Mullen, 2002: The sensitivity of the numerical simulation of the southwest monsoon boundary layer to the choice of PBL turbulence parameterization in MM5. *Wea. Forecasting*, **17**, 99–114, https://doi.org/10.1175/1520-0434(2002)017<0099:TSOTNS>2.0.CO;2.
- Brooks, I. M., 2003: Finding boundary layer top: Application of a wavelet covariance transform to lidar backscatter profiles. *J. Atmos. Oceanic Technol.*, **20**, 1092–1105, https://doi.org/10.1175/1520-0426(2003)020<1092:FBLTAO>2.0.CO;2.
- Browning, K. A., and Coauthors, 2007: The convective storm initiation project. *Bull. Amer. Meteor. Soc.*, **88**, 1939–1956, https://doi.org/10.1175/BAMS-88-12-1939.
- Ching, J. K. S., S. T. Shipley, and E. V. Browell, 1988: Evidence for cloud venting of mixed layer ozone and aerosols. *Atmos. Environ.*, 22, 225–242, https://doi.org/10.1016/0004-6981(88)90030-3.
- Clements, C. B., and Coauthors, 2007: Observing the dynamics of wildland grass fires: Fireflux—A field validation experiment. *Bull. Amer. Meteor. Soc.*, 88, 1369–1382, https://doi.org/10. 1175/BAMS-88-9-1369.
- Cohn, S. A., and W. M. Angevine, 2000: Boundary layer height and entrainment zone thickness measured by lidars and windprofiling radars. J. Appl. Meteor., 39, 1233–1247, https://doi.org/ 10.1175/1520-0450(2000)039<1233:BLHAEZ>2.0.CO;2.
- Compton, J. C., R. Delgado, T. A. Berkoff, and R. M. Hoff, 2013: Determination of planetary boundary layer height on short spatial and temporal scales: A demonstration of the covariance wavelet transform in ground-based wind profiler and lidar measurements. J. Atmos. Oceanic Technol., 30, 1566– 1575, https://doi.org/10.1175/JTECH-D-12-00116.1.
- Crook, N. A., 1996: Sensitivity of moist convection forced by boundary layer processes to low-level thermodynamic fields. *Mon. Wea. Rev.*, 124, 1767–1785, https://doi.org/10.1175/1520-0493(1996)124<1767:SOMCFB>2.0.CO;2.
- Cunningham, J. G., W. D. Zittel, R. R. Lee, R. L. Ice, and N. P. Hoban, 2013: Methods for identifying systematic differential reflectivity (Z<sub>DR</sub>) biases on the operational WSR-88D network. 36th Conf. on Radar Meteorology, Breckinridge, CO, Amer. Meteor. Soc., 9B.5, http://ams.confex.com/ams/36Radar/webprogram/Manuscript/Paper228792/JCunningham\_36thRadarConf\_9B5.pdf.
- Dabberdt, W. F., and Coauthors, 2004: Meteorological research needs for improved air quality forecasting: Report of the 11th prospectus development team of the U.S. weather research program. *Bull. Amer. Meteor. Soc.*, 85, 563–586, https://doi.org/10.1175/BAMS-85-4-563.
- Daubechies, I., 1992: Ten Lectures on Wavelets. Society for Industrial and Applied Mathematics, 357 pp.
- Doviak, R. J., and D. S. Zrnić, 1993: Doppler Radar and Weather Observations. 2nd ed. Academic Press, 562 pp.
- Du, P., W. A. Kibbe, and S. M. Lin, 2006: Improved peak detection in mass spectrum by incorporating continuous wavelet transform-based pattern matching. *Bioinformatics*, 22, 2059–2065, https://doi.org/10.1093/bioinformatics/btl355.
- Erickson, M. J., J. J. Charney, and B. A. Colle, 2016: Development of a fire weather index using meteorological observations within the northeast United States. *J. Appl. Meteor. Climatol.*, **55**, 389–402, https://doi.org/10.1175/JAMC-D-15-0046.1.

- Gamage, N., and C. Hagelberg, 1993: Detection and analysis of microfronts and associated coherent events using localized transforms. J. Atmos. Sci., 50, 750–756, https://doi.org/10.1175/ 1520-0469(1993)050<0750:DAAOMA>2.0.CO;2.
- Garc, J. A., M. L. Cancillo, and J. L. Cano, 2002: A case study of the morning evolution of the convective boundary layer depth. J. Appl. Meteor., 41, 1053–1059, https://doi.org/10.1175/ 1520-0450(2002)041<1053:ACSOTM>2.0.CO;2.
- Heinselman, P. L., P. L. Spencer, K. L. Elmore, D. J. Stensrud, R. M. Hluchan, and P. C. Burke, 2009: Radar reflectivity–based estimates of mixed layer depth. J. Atmos. Oceanic Technol., 26, 229–239, https://doi.org/10.1175/2008JTECHA1091.1.
- Holzworth, G. C., 1964: Estimates of mean maximum mixing depths in the contiguous United States. *Mon. Wea. Rev.*, 92, 235–242, https://doi.org/10.1175/1520-0493(1964)092<0235: EOMMMD>2.3.CO:2.
- Johnson, R. H., and B. E. Mapes, 2001: Mesoscale processes and severe convective weather. Severe Convective Storms, Meteor. Monogr., No. 50, Amer. Meteor. Soc., 71–122, https://doi.org/ 10.1175/0065-9401-28.50.71.
- Kumjian, M. R., 2013: Principles and applications of dual-polarization weather radar. Part II: Warm- and cold-season applications. J. Oper. Meteor., 1, 243–264, https://doi.org/10.15191/nwajom. 2013.0120
- —, A. V. Ryzhkov, H. D. Reeves, and T. J. Schuur, 2013: A dual-polarization radar signature of hydrometeor refreezing in winter storms. *J. Appl. Meteor. Climatol.*, **52**, 2549–2566, https://doi.org/10.1175/JAMC-D-12-0311.1.
- Liu, C., and Coauthors, 2020: Vertical distribution of PM<sub>2.5</sub> and interactions with the atmospheric boundary layer during the development stage of a heavy haze pollution event. *Sci. Total Environ.*, **704**, 135329, https://doi.org/10.1016/j.scitotenv.2019. 135329.
- Markowski, P. M., Y. P. Richardson, S. J. Richardson, and A. Petersson, 2018: Aboveground thermodynamic observations in convective storms from balloonborne probes acting as pseudo-Lagrangian drifters. *Bull. Amer. Meteor. Soc.*, 99, 711–724, https://doi.org/10.1175/BAMS-D-17-0204.1.
- McCaul, E. W., Jr., and C. Cohen, 2002: The impact on simulated storm structure and intensity of variations in the mixed layer and moist layer depths. *Mon. Wea. Rev.*, **130**, 1722–1748, https://doi.org/10.1175/1520-0493(2002)130<1722:TIOSSS> 2.0.CO;2.
- Melnikov, V. M., and D. S. Zrnić, 2017: Observations of convective thermals with weather radar. *J. Atmos. Oceanic Technol.*, 34, 1585–1590, https://doi.org/10.1175/JTECH-D-17-0068.1.
- —, R. J. Doviak, D. S. Zrnić, and D. J. Stensrud, 2011: Mapping Bragg scatter with a polarimetric WSR-88D. J. Atmos. Oceanic Technol., 28, 1273–1285, https://doi.org/10.1175/JTECH-D-10-05048.1.
- ——, ——, and ——, 2013: Structures of Bragg scatter observed with the polarimetric WSR-88D. *J. Atmos. Oceanic Technol.*, **30**, 1253–1258, https://doi.org/10.1175/JTECH-D-12-00210.1.
- Münkel, C., N. Eresmaa, J. Räsänen, and A. Karppinen, 2007: Retrieval of mixing height and dust concentration with lidar ceilometer. *Bound.-Layer Meteor.*, 124, 117–128, https://doi. org/10.1007/s10546-006-9103-3.
- NCEI, 2024: Annual National Climate Report. Accessed 7 May 2024, https://www.ncei.noaa.gov/access/monitoring/monthlyreport.
- NEXRAD Radar Operations Center, 2023: WSR-88D. Accessed 13 June 2023, https://www.roc.noaa.gov/WSR88D/Maps.aspx.

- Richardson, L. M., J. G. Cunningham, W. D. Zittel, R. R. Lee, R. L. Ice, V. M. Melnikov, N. P. Hoban, and J. G. Gebauer, 2017a: Bragg scatter detection by the WSR-88D. Part I: Algorithm development. J. Atmos. Oceanic Technol., 34, 465– 478, https://doi.org/10.1175/JTECH-D-16-0030.1.
- ——, W. D. Zittel, R. R. Lee, V. M. Melnikov, R. L. Ice, and J. G. Cunningham, 2017b: Bragg scatter detection by the WSR-88D. Part II: Assessment of Z<sub>DR</sub> bias estimation. J. Atmos. Oceanic Technol., 34, 479–493, https://doi.org/10.1175/ JTECH-D-16-0031.1.
- Ryan, H., O. Ricker, and B. A. Klauder, 1994: A choice of wavelets. CSEG Rec., 19, 8–9.
- Ryzhkov, A., P. Zhang, H. Reeves, M. Kumjian, T. Tschallener, S. Trömel, and C. Simmer, 2016: Quasi-vertical profiles—A new way to look at polarimetric radar data. *J. Atmos. Oceanic Technol.*, 33, 551–562, https://doi.org/10.1175/JTECH-D-15-0020.1.
- Seidel, D. J., C. O. Ao, and K. Li, 2010: Estimating climatological planetary boundary layer heights from radiosonde observations: Comparison of methods and uncertainty analysis. J. Geophys. Res., 115, D16113, https://doi.org/10.1029/2009JD013680.
- Seliga, T. A., and V. Bringi, 1976: Potential use of radar differential reflectivity measurements at orthogonal polarizations for measuring precipitation. *J. Appl. Meteor.*, 15, 69–76, https://doi.org/10.1175/1520-0450(1976)015<0069:PUORDR>2.0. CO:2.
- Stouffer, B. C., C. L. Comer, and D. Stensrud, 2024: Windsond launch data – CBL observations. Penn State Data Commons, accessed 29 May 2024, https://doi.org/10.26208/5NN6-KV44.

- Stull, R. B., 1988: An Introduction to Boundary Layer Meteorology. Kluwer Academic, 666 pp.
- Torrence, C., and G. P. Compo, 1998: A practical guide to wavelet analysis. *Bull. Amer. Meteor. Soc.*, 79, 61–78, https://doi.org/ 10.1175/1520-0477(1998)079<0061:APGTWA>2.0.CO;2.
- U.S. Department of Commerce, 2023: Maps of the NWS Rawinsonde Network. Accessed 13 June 2023, https://www.weather. gov/upperair/nws\_upper.
- White, A., 1993: Mixing depth detection using 915-MHz radar reflectivity data. Preprints, Eighth Symp. on Meteorological Observations and Instrumentation, Anaheim, CA, Amer. Meteor. Soc., 248–250.
- Wyngaard, J. C., 1985: Structure of the planetary boundary layer and implications for its modeling. J. Climate Appl. Meteor., 24, 1131–1142, https://doi.org/10.1175/1520-0450(1985)024<1131: SOTPBL>2.0.CO:2.
- Zhang, D., J. Comstock, and V. Morris, 2022: Comparison of planetary boundary layer height from ceilometer with ARM radiosonde data. *Atmos. Meas. Tech.*, 15, 4735–4749, https:// doi.org/10.5194/amt-15-4735-2022.
- Zittel, W. D., J. G. Cunningham, R. R. Lee, L. M. Richardson, R. L. Ice, and V. Melnikov, 2014: Use of hydrometeors, Bragg scatter, and sun spikes to determine system Z<sub>DR</sub> biases in the WSR-88D fleet. Eighth European Conf. Radar in Meteorology and Hydrology, Garmisch-Partenkirchen, Germany, ERAD, 25 pp., https://www.pa.op.dlr.de/erad2014/programme/ExtendedAbstracts/132 Zittel.pdf.
- Zrnić, D. S., and A. V. Ryzhkov, 2004: Polarimetric properties of chaff. J. Atmos. Oceanic Technol., 21, 1017–1024, https://doi. org/10.1175/1520-0426(2004)021<1017:PPOC>2.0.CO;2.